Backbone Dynamics of the Calcium-Signaling Protein apo-S100B as Determined by ^{15}N NMR Relaxation†

Keith G. Inman,‡ Donna M. Baldisseri,‡ Kristine E. Miller,§ and David J. Weber*,‡

University of Maryland School of Medicine, Department of Biochemistry and Molecular Biology, Baltimore, Maryland 21201, and Goucher College, Department of Chemistry, Baltimore, Maryland 21204

Received December 1, 2000

ABSTRACT: Backbone dynamics of homodimeric apo-S100B were studied by ^{15}N nuclear magnetic resonance relaxation at 9.4 and 14.1 T. Longitudinal relaxation (T_1), transverse relaxation (T_2), and the ^{15}N-{^{1}H} NOE were measured for 80 of 91 backbone amide groups. Internal motional parameters were determined from the relaxation data using the model-free formalism while accounting for diffusion anisotropy. Rotational diffusion of the symmetric homodimer has moderate but statistically significant prolate axial anisotropy ($D_\parallel/D_\perp = 1.15 \pm 0.02$), a global correlation time of $\tau_m = 7.80 \pm 0.03$ ns, and a unique axis in the plane normal to the molecular symmetry axis. Of 29 residues at the dimer interface (helices 1 and 4), only one has measurable internal motion (Q71), and the order parameters of the remaining 28 were the highest in the protein ($S^2 = 0.80$ to 0.91). Order parameters in the typical EF hand calcium-binding loop ($S^2 = 0.73$ to 0.87) were slightly lower than in the pseudo-EF hand ($S^2 = 0.75$ to 0.89), and effective internal correlation times, τ_e, distinct from global tumbling, were detected in the calcium-binding loops. Helix 3, which undergoes a large, calcium-induced conformational change necessary for target-protein binding, does not show evidence of interchanging between the apo and Ca^{2+}-bound orientations in the absence of calcium but has rapid motion in several residues throughout the helix ($S^2 = 0.78$ to 0.88; $10 \leq \tau_e \leq 30$ ps). The lowest order parameters were found in the C-terminal tail ($S^2 = 0.62$ to 0.83). Large values for chemical exchange also occur in this loop and in regions nearby in space to the highly mobile C-terminal loop, consistent with exchange broadening effects observed.

S100B is a Ca^{2+}-binding protein and a member of the highly conserved S100 protein family. The name S100 was given to these proteins because of their characteristic solubility in 100%-saturated ammonium sulfate (*1*). Over twenty S100 proteins have been identified, with distinct functions and tissue distributions (*2*−*6*). S100B, also termed S100B($\beta\beta$),[1] is a symmetric homodimer with 91 residues per S100β subunit, and it has only a few points of nonidentity in its sequence when compared among a number of mammalian sources (*7*). As is the case for several S100 family members, each subunit of S100B undergoes a large change in protein conformation upon binding Ca^{2+} (*8*−*10*). This conformational change is required, in most cases, for binding protein targets and eliciting a downstream biological response (*7*).

There are two helix−turn−helix Ca^{2+}-binding motifs per S100β subunit (*11*). The N-terminal Ca^{2+}-binding site (residues 18−31) is a *pseudo-EF hand* (ψ-EF) or *S100-hand* and has 14 residues that represent the distinguishing amino acid sequence of the S100 family. The 12-residue Ca^{2+}-binding site in the C-terminus (residues 61−72) is that of a typical or canonical EF hand as found in proteins such as calmodulin, parvalbumin, and troponin C (*12*). The affinity for Ca^{2+} in each of these sites varies widely for different S100 proteins ($0.1\ \mu M < K_D < 50\ \mu M$). In S100B, the typical EF hand binds Ca^{2+} in vitro about 10 times more tightly ($K_D \approx 20\ \mu M$) than the ψ-EF hand ($K_D \approx 200\ \mu M$) (*13*).

At present, the 3D structure is available at high resolution in the apo-state for three dimeric S100 proteins including S100B, S100A6, and S100A10 (*14*−*16*). In these structures, the orientation of the helices at the subunit interface is nearly identical with helices 1 and 4 joined nonconvalently (S100B, $K_D < 1$ nM) and antiparallel to helices 1′ and 4′ of the opposing subunit forming an X-type four helix bundle at the protein's core (*6*, *17*). The surfaces of these proteins each have a large number of hydrophilic residues. The hydrophobic core and highly polar surface provide for the high stability and solubility observed in the S100 protein family.

Comparisons of the apo- and Ca^{2+}-bound structures are important for distinguishing how different S100 proteins bind their respective protein targets to elicit unique biological effects (*6*, *18*, *19*). For example, when Ca^{2+} binds to S100B,

† This work was supported by NIH Grant GM58888 to D.J.W.

* To whom correspondence should be addressed: Dr. David J. Weber, Associate Professor, Department of Biochemistry and Molecular Biology, University of Maryland School of Medicine, 108 N. Greene St., Baltimore, MD 21201, Phone: (410) 706−4354, Fax: (410) 706−0458, E-mail: dweber@umaryland.edu.

‡ University of Maryland School of Medicine.

§ Goucher College.

[1] Abbreviations: DTT, dithiothreitol; S100β, subunit of dimeric S100B; S100B($\beta\beta$), dimeric S100B with noncovalent interactions at the dimer interface; sNTnC, N-terminal domain of skeletal troponin C; PKC, protein kinase C; RMSD, root-mean-square difference; NOE, nuclear Overhauser effect; NMR, nuclear magnetic resonance; HSQC, heteronuclear single quantum coherence; TPPI time-proportional phase incrementation; ψ-EF, pseudo-EF hand.

10.1021/bi0027478 CCC: $20.00
Published on Web 02/28/2001

helix 3 in each subunit reorients by over 90° with virtually no reorganization of the dimer-forming helices (helices 1, 4) or helix 2 (20). A smaller change in the position of helix 3 is observed for S100A6 upon Ca^{2+}-binding (*15*). In each case, however, the movement of helix 3, upon binding Ca^{2+}, exposes a unique patch of residues that are involved in binding to specific protein targets. For S100B, the Ca^{2+}-dependent interaction with the C-terminus of p53 was found to sterically block the protein kinase C (PKC) dependent phosphorylation of the tumor suppressor, which is necessary for the activation of p53 and its downstream function (*21*−*23*). In contrast, S100A10 does not bind Ca^{2+}; yet, in the absence of divalent metal, this protein has a structure that is very similar to the Ca^{2+}-loaded forms of S100B and S100A6. Target proteins such as annexin II, therefore, bind to S100A10 in a Ca^{2+}-independent manner (*16*).

It is not clear how different EF hand containing proteins give such a diverse range of structural and thermodynamic responses to calcium and protein targets, given their high degree of homology. How these proteins "fine-tune" their responses to Ca^{2+} and protein targets can be better understood when their 3D structures are complemented by detailed descriptions of internal dynamics. Prior to this work, calbindin D_{9k} was the only S100 protein for which internal dynamics had been extensively studied (*24*, *25*). While those studies were paramount to the understanding of protein dynamics in general, and more specifically to Ca^{2+}-binding proteins, their results cannot be generalized to the S100 family. Calbindin is atypical among S100 proteins, since it is the only one that exists as a monomer, and it exhibits no Ca^{2+}-dependent conformational change. Moreover, calbindin is truncated at the C-terminus in comparison to other S100 proteins and does not bind any known protein targets. Therefore, to characterize further this important class of Ca^{2+}-binding proteins, we report here the internal dynamics of a more typical, dimeric S100 protein, S100B($\beta\beta$). Our results indicate that the dimer interface of S100B has very little motion in the absence of Ca^{2+}, which helps to explain its high stability. However, regions of apo-S100B that interact subsequently with Ca^{2+} and target proteins exhibit more complicated dynamics, on multiple time scales. A preliminary abstract of this work has been published (*26*).

MATERIALS AND METHODS

Materials. Perdeuterated tris (>98.7 atom % D) was purchased from C/D/N Isotopes, Inc. (Vandreuil, Quebec), and D_2O (>99.9 atom % D, low in paramagnetic impurities) and $^{15}NH_4Cl$ (>99 atom % ^{15}N) was purchased from Cambridge Isotope Laboratories (Woburn, Mass.). Other materials were of the highest quality commercially available. Buffers were passed through Chelex-100 resin (BioRad) to remove trace metals.

Sample Preparation. ^{15}N-labeled S100B was overexpressed and purified from *Escherichia coli* as previously described (*14*). NMR samples were 3 mM S100β (subunit concentration), 10 mM tris-d_{11}, 15 mM NaCl, 0.1 mM EDTA, 5 mM DTT, 0.35 mM NaN_3, 10% D_2O, pH 6.50. Samples were degassed by vacuum and argon replacement shortly before each set of experiments.

NMR Data Collection. Experiments were performed on Bruker Avance DMX-600 and DRX-400 NMR spectrometers at 37.0 °C, calibrated with neat ethylene glycol on each instrument. Longitudinal relaxation (T_1) experiments were performed using sensitivity-enhanced inversion−recovery pulse sequences with pulsed field gradients (*27*). Each spectrum was acquired with 512* (t_2) × 64* (t_1) points, with sweep widths of 8400 Hz in ^1H and 1338 Hz in ^{15}N and 32 scans per t_1 point at 600 MHz. At 400 MHz, sweep widths were 5593 Hz (^1H) by 893 Hz (^{15}N), using 48 scans per t_1 point. A recycle delay of 3.2 s was employed at both fields. Delay times of 30 (×2), 110, 240, 480, 960, 1500, and 2940 ms were used at 600 MHz, and 30, 70 (×2), 130, 280, 560, 1130, and 2250 ms at 400 MHz. Transverse relaxation (T_2) experiments were performed using sensitivity-enhanced CPMG pulse sequences with pulsed field gradients (*27*). Acquisition parameters were identical to those of the T_1 experiments, except 64 scans were collected per t_1 point at 400 MHz, and recycle delays were 3.3 s at 600 MHz and 3.0 s at 400 MHz. Delay times of 8 (×2), 32, 88, 184 (×2), and 312 ms were used at 600 MHz, and 8 (×3), 16, 32, 64, 128 (×3), 256, and 512 ms at 400 MHz. ^{15}N-{^1H} NOE ratios were measured by fully interleaving the NOE and reference experiments as previously described (*27*). The NOE experiment used a 3-s presaturation period and a 2-s relaxation delay; the control experiment had an equivalent 5-s delay. In these experiments, water was returned to the *z*-axis prior to each scan to avoid saturation transfer (*27*). Both NOE and control experiments were acquired with 512* (t_2) × 160* (t_1) (600 MHz) or 512* (t_2) × 100* (t_1) (400 MHz) points, with 48 scans at 600 MHz and 20 scans at 400 MHz.

NMR Data Processing and Analysis. All NMR data were processed and analyzed with NMRPipe and NMRDraw software (*28*). Spectra were extended by linear prediction and zero-filling prior to apodization with a 5%-shifted mixed Gaussian/exponential function. Peak heights for the relaxation series were measured by fitting Gaussian surfaces to the transformed data and taking the maximum height of the fitted surface using the program NlinLS (*28*). The jackknife procedure (*29*) was used with the Levenberg−Marquardt nonlinear least squares algorithm (*30*) to fit peak heights as a function of relaxation delay with the two-parameter exponential, $I = I_0 \exp[-Rt]$, where R is either $R_1 = 1/T_1$ or $R_2 = 1/T_2$, using the computer program CURVEFIT (A. G. Palmer, Columbia University). NOE peak heights were taken from similarly derived Gaussian fits to the frequency-domain data. The NOE was calculated as $\mathrm{NOE} = \eta + 1 = I_{\mathrm{presat}}/I_{\mathrm{no-presat}}$, where I_{presat} and $I_{\mathrm{no-presat}}$ are the peak heights with and without ^1H presaturation, respectively.

Rotational Diffusion Anisotropy. Overall rotation of the molecule was analyzed to separate its contributions to relaxation from those of site-specific internal motions. Residue-specific correlation times, τ_{loc}, were derived from T_1/T_2 values (*31*) (software R2R1_TM, A. G. Palmer, Columbia University), and a single, isotropic correlation time for the protein was calculated as their trimmed mean. The small degree of anisotropy expected for S100B($\beta\beta$) permitted a quadric approximation of the dependence of local correlation times on individual bond orientations in the diffusion frame (*32*). Estimates of axial and fully anisotropic diffusion tensors were then obtained by applying minimization techniques to this relation (software QUADRIC_DIFFUSION, v1.11; A. G. Palmer). Residues for which NOE < 0.65 at

600 MHz or was not known were eliminated from consideration for this analysis, due to possible fast internal motions. Furthermore, the criterion (*33*)

$$\frac{\langle T_2\rangle - T_{2,i}}{\langle T_2\rangle} - \frac{\langle T_1\rangle - T_{1,i}}{\langle T_1\rangle} < 1.5 \times \mathrm{SD} \qquad (1)$$

was applied to the remaining residues, where SD is the standard deviation of the collection of values of the left side for all residues considered, using 600 MHz data. Residues not satisfying the inequality were eliminated from this stage of the analysis due to possible exchange contributions to T_2 relaxation. Isotropic Brownian rotation was characterized by a single diffusion coefficient, D, or rotational correlation time, $\tau_m = (6D)^{-1}$. Alternatively, a 2nd rank ellipsoidal tensor was used to model diffusion as either axially symmetric (four parameters) or fully anisotropic (six parameters). Axially symmetric diffusion was described by an isotropic correlation time, $\tau_m = (6D_{iso})^{-1}$, a shape factor $D_\parallel/D_\perp$ and two Euler angles Θ and Φ, to represent the orientation of the unique axis of the diffusion tensor in the molecular frame; $D_{iso} = (D_\parallel + 2D_\perp)/3$, and $D_\parallel$ and $D_\perp$ are the diffusion coefficients parallel and perpendicular to the unique axis, respectively. Fully anisotropic rotation was modeled using three diffusion coefficients, D_{xx}, D_{yy}, and D_{zz}, or alternatively by $D_{iso} = (D_{xx} + D_{yy} + D_{zz})/3$ and two shape factors, $2D_{zz}/(D_{xx} + D_{yy})$ and D_{xx}/D_{yy}. Three Euler angles, Θ, Φ, and Ψ, defined the orientation of the fully anisotropic diffusion tensor. Isotropic, axially symmetric, and fully anisotropic rotational models were subjected to statistical F-testing as previously described (*34*). Atomic coordinates (PDB accession code: 1B4C) used throughout this study were those of a high-resolution structure derived in part from residual dipolar coupling constraints (*14*). Coordinates were transformed so that the center of mass of the homodimer was at the origin, and the principal axes of the point-mass rotational inertia tensor, calculated without hydration, were aligned with the coordinate axes (software PDB_INERTIA version 1.1, A. G. Palmer, Columbia University). The principal axis of the inertia tensor was thus the z-axis of the transformed coordinate frame, with the x-axis as the C_2 dimer symmetry axis; these coordinates are referred to as the *molecular frame*.

Model-Free Analysis. A complete model-free analysis of internal motion and overall rotational diffusion was performed using the program MODELFREE (v4.1, A. G. Palmer, Columbia University) (*35*, *36*). A spectral density function was chosen to reflect an axially symmetric diffusion tensor, and site-specific motion on as many as two timescales (*35*, *37*, *38*):

$$J(\omega) = \frac{2}{5}\sum_{j=1}^{3} A_j\left[\frac{S^2\tau_j}{1+(\omega\tau_j)^2} + \frac{(1-S_f^2)\tau_f'}{1+(\omega\tau_f')^2} + \frac{(S_f^2-S^2)\tau_s'}{1+(\omega\tau_s')^2}\right] \qquad (2)$$

where $S = S_fS_s$ is the model-independent or *generalized* order parameter of the model-free formalism, S_f and S_s are order parameters on the fast ($\tau_f < \sim 200$ ps) and slow ($\tau_s > \sim 200$ ps) time scales, respectively; $\tau_1^{-1} = 6D_\perp$, $\tau_2^{-1} = D_\parallel + 5D_\perp$, and $\tau_3^{-1} = 4D_\parallel + 2D_\perp$; $\tau_s' = \tau_j\tau_e/(\tau_j + \tau_e)$, where τ_e is either τ_s or τ_f; $A_1 = (3\cos^2\theta - 1)^2/4$, $A_2 = 3\sin^2\theta\cos^2\theta$, $A_3 = (3/4)\sin^4\theta$, and θ is the angle between the N-H bond vector and the unique axis of the diffusion tensor. Fast internal motions are defined as those for which $\tau/(1 + \omega^2\tau^2)$ is within 10% of τ_e, where $\tau = \tau_m\tau_e/(\tau_m + \tau_e)$ (*35*). Several simplifying assumptions regarding $J(\omega)$ were applied where the data permitted, giving rise to a number of mathematical models for characterizing internal motion. In keeping with standard practice, model 1 assumes that slow internal motions are negligible ($S_s^2 = 1$) and that fast motions are very fast ($\tau_f <$ 20 ps), so as to contribute negligibly to the spectral density function, and thus reduces $J(\omega)$ to

$$J(\omega) = \frac{2}{5}\sum_{j=1}^{3} A_j\left[\frac{S_f^2\tau_j}{1+(\omega\tau_j)^2}\right] \qquad (2a)$$

allowing only S_f^2 to be optimized, in addition to global diffusion parameters. Model 2 assumes only that slow internal motions are negligible ($S_s^2 = 1$), resulting in

$$J(\omega) = \frac{2}{5}\sum_{j=1}^{3} A_j\left[\frac{S_f^2\tau_j}{1+(\omega\tau_j)^2} + \frac{(1-S_f^2)\tau_f'}{1+(\omega\tau_f')^2}\right] \qquad (2b)$$

which allows both an order parameter, S_f^2, and a correlation time, $\tau_e = \tau_f$ to be derived from the data. Model 5 assumes that fast internal motions are very fast ($\tau_f \rightarrow 0$), giving

$$J(\omega) = \frac{2}{5}\sum_{j=1}^{3} A_j\left[\frac{S^2\tau_j}{1+(\omega\tau_j)^2} + \frac{(S_f^2-S^2)\tau_s'}{1+(\omega\tau_s')^2}\right] \qquad (2c)$$

which allows for optimizing order parameters on two time scales, S_f and S_s, such that $S = S_fS_s$, as well as a correlation time $\tau_e = \tau_s$, for slow internal motions. It should be noted that internal motions on the slow internal time scale are not in the extreme narrowing limit of $\omega\tau \ll 1$, which compromises the accuracy of order parameters derived from models 5 and 6 (*35*). Models 3, 4, and 6 are obtained from 1, 2, and 5, respectively, by allowing an exchange contribution to transverse relaxation.

A set of well-known equations were used to relate relaxation rate data to rotation of the amide $^1H-^{15}N$ bond vector (*31*, *39*):

$$R_1 = \frac{d^2}{4}[3J(\omega_N) + J(\omega_H - \omega_N) + 6J(\omega_H + \omega_N)] + c^2J(\omega_N)$$

$$R_2^0 = \frac{d^2}{8}[4J(0) + 3J(\omega_N) + J(\omega_H - \omega_N) + 6J(\omega_H) + 6J(\omega_H + \omega_N)] + \frac{c^2}{6}[4J(0) + 3J(\omega_N)] \qquad (3)$$

$$\mathrm{NOE} = 1 + \frac{d^2}{4}\frac{\gamma_H}{\gamma_N}[6J(\omega_H + \omega_N) - J(\omega_H - \omega_N)]T_1$$

where $d = \mu_0 h\gamma_H\gamma_N/(8\pi^2 r_{NH}^3)$, $c = \omega_N\Delta\sigma/\sqrt{3}$, μ_0 is the permeability of free space, h is Planck's constant, ω_X and γ_X are the Larmor frequency and gyromagnetic ratio, respectively, for nucleus X, r_{NH} is the N-H internuclear distance, assumed to be 1.02 Å, $\Delta\sigma = \sigma_\parallel - \sigma_\perp$ is the chemical shift anisotropy (CSA), taken to be -170 ppm (*40*),

and $\sigma_{||}$ and $\sigma_{\perp}$ are parallel and perpendicular components of the axially symmetric ellipsoidal ^{15}N chemical shift tensor, with a principal axis assumed to be parallel to the ^{1}H-^{15}N bond vector.

Using the initial estimate of the diffusion tensor resulting from the quadric analysis, eqs 2 and 3 were fitted to the R_1, R_2, and NOE data at both fields for each residue. A model was selected for each residue, following closely the procedure of Mandel et al. (*41*) except that having data at two fields allowed the use of a four-parameter model (model 6) for certain residues. Also, *F*-testing could be performed for all higher model comparisons, because of the extra degrees of freedom afforded by having data collected at more than one field strength. Statistical χ^2-testing was performed at the $p = 0.1$ level of significance and *F*-testing was performed at $p = 0.2$. For each residue, the simplest model to pass such criteria was used. Global diffusion parameters were optimized along with internal motion using only those residues for which models 1−4 were accepted.[2] Residues from the C-terminal tail (*84*−*91*) were excluded from the diffusion optimization runs to avoid adverse effects from their increased local mobility. After each global optimization, model selection was repeated holding the resulting diffusion tensor fixed, followed by another optimization of global diffusion, and so on, until diffusion parameters and model selection converged. Finally, the highly mobile C-terminal residues 88−91 were analyzed by allowing each to have a unique rotational correlation time, τ_{loc}, since the motions in these residues were expected to be fairly independent of overall reorientation of the molecule.

Error Analysis. Error in peak heights was determined by pairwise comparison of duplicate experiments, taking the standard deviation of peak height to be the standard deviation of the pairwise differences, divided by $\sqrt{2}$ (*42*). In the relaxation series, not all of the delay times were duplicated, so it was assumed that peak-height uncertainty varied in proportion to the baseline noise, which was validated by performing more than one pair of duplicates in two of the four series. Median reduced χ^2 values for the exponential fits were 0.15 for T_1^{600}, 0.46 for T_2^{600}, 0.16 for T_1^{400}, and 0.15 for T_2^{400}, which are lower than expected. Uncertainties for R_1 and R_2 were determined by the jackknife procedure using the computer program CURVEFIT (v1.2, A. G. Palmer, Columbia University) and were then adjusted for each series to achieve a proper χ^2 distribution, giving a 10%-trimmed mean error of less than 1%. When fitting relaxation data with the model-free equations, these low estimates of error in R_1 and R_2 did not allow the use of simple models for more than a few residues. Therefore, uncertainties in R_1 and R_2 data were uniformly scaled so that models that included exchange (models 3, 4, or 6) were chosen for residues identified experimentally as undergoing chemical exchange, and so that models with internal correlation times were assigned to residues with clear evidence of rapid internal motion (low NOE values). Exchange was considered likely in residues that were broadened, had high T_1/T_2 ratios, or deviated from a linear correlation between T_1/T_2 vs amide-proton residual dipolar coupling values (*43*). With these estimates, trimmed mean error for each R_1 and R_2 data set was approximately 2.5 to 3%, and these estimates were used for subsequent iterations of the model-free analysis. The NOE data was collected in duplicate at 400 and 600 MHz, and the errors were of reasonable magnitude (average ± 0.02 at 600 MHz and ± 0.03 at 400 MHz).

To explore effects of anisotropy on the internal dynamics results, particularly the possibility of introducing complex models where not appropriate, the model-free analysis was repeated twice, either under the assumption of isotropic tumbling or by modeling the diffusion tensor as oblate axial. The isotropic correlation time, τ_{iso} was 7.99 ns, and the oblate tensor was $\tau_m = 7.89$ ns and $D_{||}/D_{\perp} = 0.84$ with an orientation coincident to the dimer symmetry axis (perpendicular to the prolate unique axis). The order parameters calculated and model selection varied only slightly from those found for the prolate model. The loss or addition of exchange terms occurred only where the acute angles to the unique axes of the two tensors differed by more than about 45°, and then only when $R_{ex}^{600} < 1$/s. However, effective internal correlation times did show differences, with more residues having nonzero τ_e and generally higher values found when the oblate tensor was used.

Independent Measurement of Rotational Diffusion. To ensure that aggregation in the concentrated NMR samples did not affect estimates of global tumbling, the isotropic coefficient of rotational diffusion, $\tau_{iso} = (6D_{iso})^{-1}$ was calculated on the basis of a Stokes' radius measured with gel filtration chromatography at nanomolar concentration (*17*), using the equation (*44*)

$$D_{iso} = \frac{RT}{8L\pi\eta r^3} \quad (4)$$

where R is the gas constant, T is the temperature, L is Avogadro's number, η is the solvent viscosity, and r is the Stokes' radius of the molecule, assumed to be spherical.

RESULTS AND DISCUSSION

Relaxation Data. Relaxation data was measured at two fields for 80 of the 91 backbone amide resonances of S100B (Figure 1 and Supporting Information). The other 11 were not measured because of overlap (I11, Q16, E21, N37, E49, K55, E72) or because correlations were missing due to exchange broadening (I47, H85, E86, F87). The 10%-trimmed mean values for R_1 (= $1/T_1$) were 1.46 s^{-1} at 600 MHz and 2.45 s^{-1} at 400 MHz. For R_2, the 10%-trimmed mean values were 10.7 s^{-1} at 600 MHz and 9.56 s^{-1} at 400 MHz, and T_1/T_2 trimmed means were 7.31 at 600 MHz and 3.88 at 400 MHz. The ^{15}N-{^{1}H} NOE values had trimmed means of 0.79 and 0.74 at 600 and 400 MHz, respectively. Lower than average NOE and R_1 values are found in the two calcium-binding loops (residues G19−K26: $R_1^{400} = 2.44$ and $NOE^{600} = 0.74$; D61−C68: $R_1^{400} = 2.32$ and $NOE^{600} = 0.73$) and at the extreme C-terminus (residues E89−E91: $R_1^{400} = 2.10$ and $NOE^{600} = 0.38$). Specific residues in these regions with NOE values noticeably below the mean are G22, D23, K24, K28, E62, D63, G64, E67, C68, and E89−E91, indicating contributions to their relax-

[2] To check whether the omission of the two-time-scale models (models 5 and 6) affected the results of global diffusion analysis, a final optimization was performed including residues assigned to all models. Although the calculations required considerably more time, the resulting diffusion tensor was indistinguishable from that obtained using only residues fitting models 1−4.

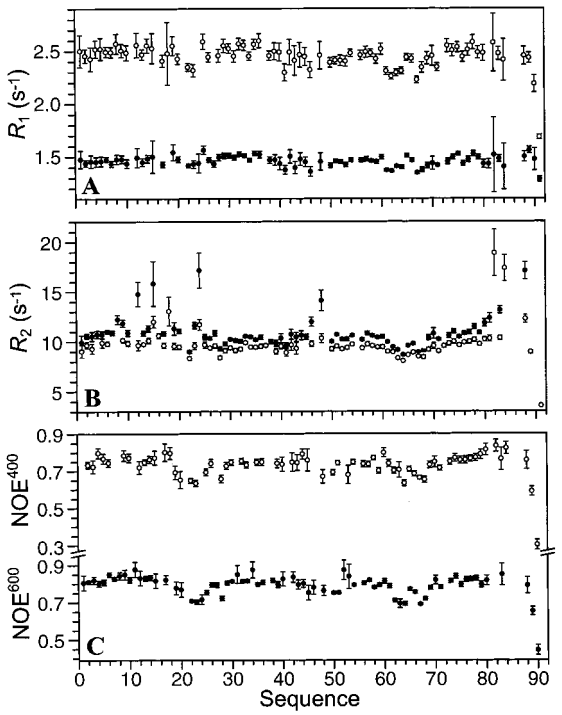

FIGURE 1: Relaxation rate data for apo-S100B($\beta\beta$). (A) Longitudinal relaxation rate, R_1, (B) transverse relaxation rate, R_2, and (C) ^{15}N-{^{1}H} heteronuclear NOE ($\eta + 1$) are given for nitrogen Larmor frequencies of 61 MHz (●) and 41 MHz (○). Larger error bars are generally due to exchange broadening, which lowers signal-to-noise ratio and consequently raises uncertainty in peak height.

ation from internal dynamics as represented by an effective internal correlation time, τ_e.

Residues with R_2^{600} values significantly higher than the mean ($R_2^{600} \geq \sim 12$/s), with lesser, similar effects at 400 MHz, included V8, A9, D12, H15, S18, K24, E46, K48, V80−C84, F88, and E89 (with R_2 measurable only at 400 MHz for S18, T82, and C84 due to severe broadening) suggesting $R_{ex} \neq 0$ for these residues. Except for E89, these same residues had noticeably higher T_1/T_2 ratios (Figure 2, panel A). With A9 as the only exception, nonzero R_{ex} values were calculated for each of the other 14 residues, using the program MODELFREE. Residual dipolar couplings measured at 600 MHz were collected previously for several amide-proton correlations in S100B($\beta\beta$) (*14*), and comparing these data to relaxation rate data can also be used to identify residues with exchange contributions (*43*). A plot of the residual dipolar couplings D_{NH} vs T_1^{600}/T_2^{600} identified D12, D23, E46, K48, V80, and A83 as having exchange contributions to T_2 relaxation (Figure 2, panel B). Three other residues (A9, L27, and D69) that appear to have small R_{ex} terms in the D_{NH} versus T_1/T_2 plot were not found to have significant exchange contributions in the model-free analysis.

Rotational Diffusion. The point-mass inertia tensor for apo-S100B (PDB accession: 1B4C) has principal moments with the ratio 1.39:1.09:1.00 (program PDBINERTIA v1.1, A. G. Palmer, Columbia University), leading to the expectation of a diffusion tensor with a small degree of axially symmetric anisotropy. Therefore, to discern effects of global rotation from those of residue-specific motions, an analysis of rotational diffusion was carried out. In this analysis, residues for which NOE^{600} < 0.65 (H90 and E91) were eliminated from consideration for the initial estimate of the diffusion tensor, due to the possibility of significant internal motion. The criterion of eq 1 further eliminated D12, H15, S18, K24, E46, K48, A83, F88, and E89, because of probable chemical exchange contributions. Either T_1^{600}, T_2^{600}, or NOE^{600} was missing for S18, N38, S41, T81, T82, and C84, so they could not be evaluated by these criteria and were eliminated from initial diffusion calculations. The T_1^{600}/T_2^{600} ratios of the remaining 64 residues were used to calculate local correlation times and estimate isotropic, axially symmetric, and fully anisotropic diffusion tensors by the quadratic method of Brüschweiler (*45*). Of those 64 residues, six did not have both T_1^{400} and T_2^{400} measurements because of a weak signal or overlap (E4, M7, V8, L27, L44, and E45). In the absence of those T_1/T_2 values the 400 MHz data resulted, nevertheless, in a diffusion tensor indistinguishable from that derived from 600 MHz data.

The choice between isotropic, axial, and fully anisotropic diffusion tensors calculated from the T_1/T_2 data was made with the statistical *F*-test (*34*). The two axial diffusion tensors fit the 600 MHz data with statistically significant ($p \ll 1$) improvement over the best isotropic correlation time of 7.86 ± 0.01 ns. One was prolate (τ_m = 7.74 ± 0.04 ns, $D_\parallel/D_\perp$ = 1.16 ± 0.01; $p < 10^{-5}$), and the other was oblate (τ_m = 7.82 ± 0.04 ns, $D_\parallel/D_\perp$ = 0.89 ± 0.01 $p < 0.03$). Each axial tensor was compared to the fully anisotropic result

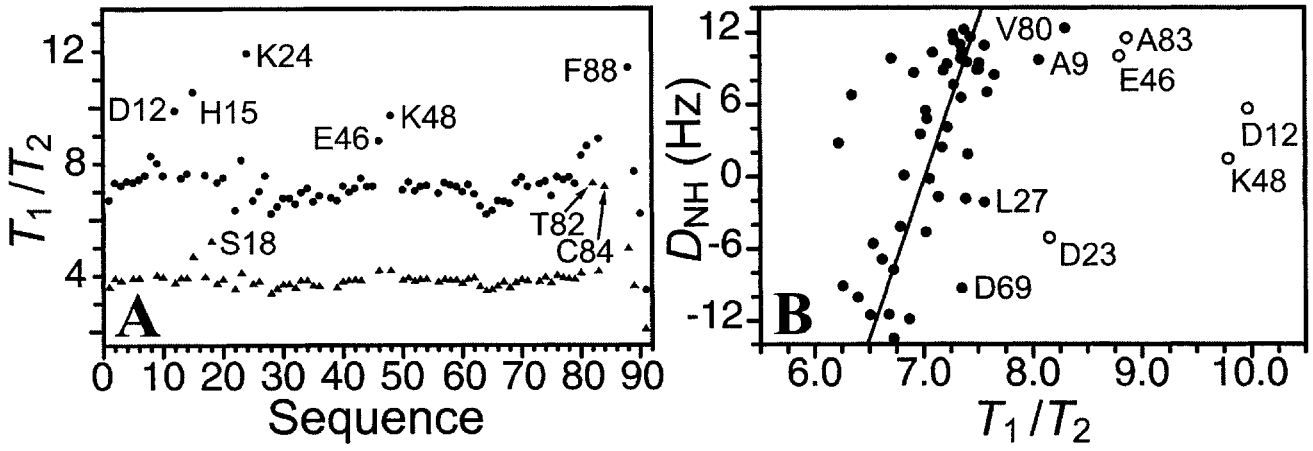

FIGURE 2: (A) ^{15}N T_1/T_2 ratios for apo-S100B($\beta\beta$) at 61 MHz (●) and 41 MHz (▲) nitrogen Larmor frequency, by sequence position. (B) 61 MHz ^{15}N T_1/T_2 ratios compared to amide proton−nitrogen residual dipolar couplings, D_{NH}, with data included in the linear correlation displayed as filled circles (●), and those considered to be outliers as open circles (○).

Table 1: Modelfree Results for apo-S100B($\beta\beta$)[a]

res	2°	model	S^2	S_s^2	τ_e	R_{ex}^{600}	res	2°	model	S^2	S_s^2	τ_e	R_{ex}^{600}
S1		1	0.85 ± 0.03				I47		X				> 0
E2		1	0.86 ± 0.01				K48		4	0.82 ± 0.04		24 ± 15	3.9 ± 1.0
L3	α	1	0.85 ± 0.02				E49		OL				
E4	α	1	0.87 ± 0.02				Q50	α	2	0.82 ± 0.01		26 ± 3	
K5	α	1	0.88 ± 0.02				E51	α	2	0.86 ± 0.01		28 ± 4	
A6	α	1	0.88 ± 0.01				V52	α	1	0.85 ± 0.01			
M7	α	3	0.85 ± 0.01			0.8 ± 0.3	V53	α	1	0.84 ± 0.01			
V8	α	3	0.87 ± 0.02			1.7 ± 0.5	D54	α	2	0.87 ± 0.01		15 ± 4	
A9	α	1	0.90 ± 0.01				K55	α	OL				
L10	α	1	0.87 ± 0.01				V56	α	2	0.85 ± 0.01		10 ± 4	
I11	α	OL					M57	α	1	0.88 ± 0.01			
D12	α	3	0.87 ± 0.03			1.9 ± 1.0	E58	α	2	0.86 ± 0.01		18 ± 4	
V13	α	1	0.87 ± 0.01				T59	α	5	0.84 ± 0.01	0.97 ± 0.01	800 ± 370	
F14	α	1	0.90 ± 0.01				**L60**	α	1	0.87 ± 0.01			
H15	α	3	0.87 ± 0.04			5.3 ± 1.5	**D61**	α	2	0.81 ± 0.01		11 ± 3	
Q16	α	OL					**E62**	α	2	0.78 ± 0.00		30 ± 2	
Y17	α	1	0.86 ± 0.01				**D63**		2	0.77 ± 0.01		34 ± 5	
S18	α	3	0.86 ± 0.10			7.7 ± 4.2	**G64**		5	0.73 ± 0.01	0.92 ± 0.01	770 ± 140	
G19		1	0.89 ± 0.02				**D65**		5	0.79 ± 0.01	0.93 ± 0.01	1600 ± 290	
R20		4	0.84 ± 0.01		34 ± 12	0.8 ± 0.3	**G66**		5	0.80 ± 0.01	0.95 ± 0.02	940 ± 260	
E21		OL					**E67**	β	2	0.76 ± 0.01		31 ± 2	
G22		5	0.76 ± 0.01	0.93 ± 0.01	700 ± 170		**C68**	β	5	0.76 ± 0.01	0.94 ± 0.01	600 ± 180	
D23		6	0.75 ± 0.03	0.92 ± 0.04	740 ± 270	2.7 ± 0.4	**D69**	β	2	0.83 ± 0.01		15 ± 4	
K24[b]		0					**F70**	α	1	0.86 ± 0.02			
H25		2	0.88 ± 0.01		42 ± 8		**Q71**	α	6	0.76 ± 0.03	0.94 ± 0.04	1900 ± 620	0.7 ± 0.3
K26	β	2	0.85 ± 0.01		13 ± 5		**E72**	α	OL				
L27	β	4	0.84 ± 0.02		11 ± 4	0.8 ± 0.3	F73	α	1	0.87 ± 0.01			
K28	β	5	0.76 ± 0.01	0.90 ± 0.02	1200 ± 230		M74	α	1	0.89 ± 0.01			
K29	α	2	0.85 ± 0.01		9 ± 4		A75	α	0				
S30	α	1	0.86 ± 0.01				F76	α	1	0.87 ± 0.01			
E31	α	1	0.85 ± 0.01				V77	α	1	0.88 ± 0.01			
L32	α	1	0.87 ± 0.01				S78	α	1	0.91 ± 0.01			
K33	α	1	0.88 ± 0.01				M79	α	1	0.88 ± 0.01			
E34	α	1	0.86 ± 0.01				V80	α	3	0.86 ± 0.02			1.2 ± 0.4
L35	α	2	0.87 ± 0.01		13 ± 4		T81	α	3	0.84 ± 0.03			2.2 ± 0.6
I36	α	1	0.88 ± 0.01				T82	α	3	0.89 ± 0.07			20.0 ± 4.4
N37	α	OL					A83	α	3	0.87 ± 0.01			1.9 ± 0.4
N38	α	1	0.84 ± 0.01				C84		3	0.83 ± 0.06			18.3 ± 3.2
E39	α	1	0.84 ± 0.01				H85		X				> 0
L40	α	1	0.86 ± 0.01				E86		X				> 0
S41		1	0.80 ± 0.01				F87		X				> 0
H42		1	0.88 ± 0.02				F88		3^{loc}	0.82 ± 0.05		τ_{loc} = 7400 ± 640	8.0 ± 1.8
F43		1	0.84 ± 0.02				E89		3^{loc}	0.67 ± 0.02		τ_{loc} = 4700 ± 240	7.3 ± 0.5
L44		1	0.87 ± 0.02				H90		3^{loc}	0.63 ± 0.02		τ_{loc} = 2100 ± 50	6.4 ± 0.6
E45		1	0.86 ± 0.01				E91		3^{loc}	0.62 ± 0.01		τ_{loc} = 1300 ± 10	3.1 ± 0.1
E46		3	0.80 ± 0.02			2.1 ± 0.5							

[a] Units for τ_e are ps and for R_{ex} are s^{-1}. Residues in bold are in the calcium-binding EF and ψ-EF hands. Secondary structural elements are given in the column marked "2°." A model choice of "0" indicates no model was deemed appropriate for the data. Relaxation rates were not measured for some residues as noted in the model choice column due to spectral overlap ("OL") or severe exchange broadening ("X"). C-terminal residues did not fit any model unless treated as though diffusing independently of the molecule, and their unique correlation times, τ_{loc}, are given in the τ_e column. [b] Although no model is appropriate for K24, there is evidence of fast internal motion (low NOE) and nonzero R_{ex} (high R_2, T_1/T_2).

(τ_m = 7.75 ± 0.07 ns, $2D_{zz}/(D_{xx} + D_{yy})$ = 1.16 ± 0.01, D_{xx}/D_{yy} = 1.015 ± 0.005). The fully anisotropic tensor was prolate-like ($2D_{zz}/(D_{xx} + D_{yy}) > 1$ and $D_{xx}/D_{yy} \approx 1$) and was better than the oblate tensor ($p < 10^{-3}$). No improvement was observed, however, when the fully anisotropic tensor was compared to the prolate axial tensor ($p \approx 0.9$) because of their similarity. Using 400 MHz data, comparable results were obtained. Furthermore, with the simultaneous use of the data at both fields, an estimation of the diffusion tensor was found to be similar using a Bayesian statistical approach (*46*). Consistent with the dimer symmetry of S100B, the orientation of the unique axis of the prolate and fully anisotropic diffusion tensors were perpendicular to the dimer symmetry axis, and that of the oblate tensor was coincident with the symmetry axis (*33*). The prolate model was chosen because it was the simplest model that was not improved by increasing the number of parameters. As expected for a low degree of axial anisotropy, the T_1/T_2 ratio showed a small dependence on N-H bond orientation relative to the principal axis of the diffusion tensor (data not shown).

The isotropic rotational correlation times derived from the relaxation data agrees well with the value calculated from a Stokes' radius of 22.6 ± 0.1 Å, measured at subnanomolar concentration (*17*). Using eq 6 and a solvent viscosity of 696 μPa·s at 37 °C, an isotropic diffusion coefficient of $D_{iso} = 21.2\ \mu s^{-1}$ was calculated, corresponding to a correlation time of 7.87 ± 0.04 ns. Agreement with the NMR result indicates that NMR sample conditions did not promote aggregation.

Model-Free Analysis. The prolate diffusion tensor derived from T_1 and T_2 data at two fields was used as an initial estimate for fitting the model-free equations (eqs 2 and 3) to the complete set of relaxation data (both fields simultaneously) using the program MODELFREE, version 4.1 (*41*).

Two rounds of model selection and diffusion tensor optimization converged, with little variation, on the final diffusion tensor ($\tau_m = 7.80 \pm 0.03$ ns, $D_\parallel/D_\perp = 1.15 \pm 0.02$ with the unique axis about 30 degrees from the inertia tensor).

Of the 80 residues for which relaxation data were obtained, models were selected for 76 using the criteria outlined in Materials and Methods. Selecting models for residues D12, E58, T59, and E62 required relaxing the χ^2-test requirement to the 0.05 level of significance and careful examination of the data. Additionally, although model 1 was selected for S18 by the statistical criteria, the resulting order parameter was unrealistically high (0.93). Exchange broadening is observed for S18, to the point where no reliable relaxation data could be collected at 600 MHz; thus, model 3 was chosen instead, and it fit the data well. Model 5 passed the selection criteria for A75 using an arbitrary value of τ_s, but τ_s failed to converge on a value less than τ_m. Model 5 parameters, τ_s, S_s, and S_f could not, therefore, be considered meaningful for A75, nor was any other model found appropriate for this residue. In summary, model 1 was selected for 37 residues, model 2 for 14 residues, model 3 for 15 residues, model 4 for 3 residues, model 5 for 7 residues, and model 6 for 2 residues (Table 1). In general, residues that required the fewest parameters to fit the relaxation rate data (models 1, 2, and 3) were in regions of α-helical structure and in loop 2, also called the *hinge*. The most complex models (models 4, 5, and 6) were required typically for residues in the Ca^{2+}-binding loops, including the β-strands (Table 1).

Dynamics of apo-S100B. The highest order parameters (0.84−0.91, excluding Q71) in apo-S100B were found at the very tight dimer interface ($K_D < 1$ nM), an X-type four-helix bundle formed by helices 1, 4, 1′, and 4′ (Figure 3, panels A and B; Table 1). Very little internal motion was detected in these helices, with nonzero τ_e and lower order parameters found only in Q71 ($S^2 = 0.76 \pm 0.03$, $\tau_s = 2$ ns) on a solvent-exposed edge of the region (Figure 3, panel B, and Figure 4, panel B). Chemical exchange is detected along one side of helix 1, with $R_{ex}^{600} > 1$/s for V8, D12, H15, and S18 (Figure 3, panel C, and Figure 4, panel C). These exchange terms do not necessarily indicate backbone motion but are likely introduced by interactions with the C-terminal loop, which is nearby and exhibits significant exchange broadening.

In the tertiary structure of S100B, residues with exchange contributions are grouped around the mobile C-terminal loop (Figure 4, panel C). Exchange is detected for all HSQC correlations from the last turn of helix 4 (V80) to the C-terminus at E91, and no correlations are observed for residues H85, E86, and F87 due to exchange broadening. Residues in the C-terminal loop can approach within a few angstroms of E46 and K48 in the linker of the same subunit. Broadening is observed for I47 to the point where relaxation rates could not be measured. Furthermore, weak NOE correlations are found between the amide proton of F88 and side-chain protons of either E45 or E46, but these were not used in the structure determination due to conformational averaging in this region (Drohat, A. C., unpublished data). No other NOE correlations were observed in the C-terminus, which supports the idea that this region of the protein is mobile on the chemical shift time scale.

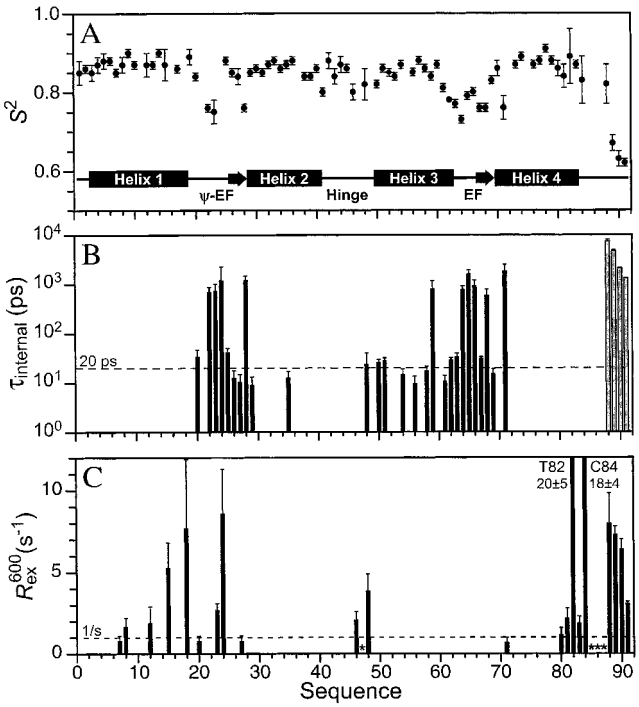

FIGURE 3: Model-free results for apo-S100B($\beta\beta$) vs sequence position. (A) Generalized order parameter, S^2, encompassing both fast and slow internal motions ($S^2 = S_f^2 S_s^2$), (B) internal correlation times, τ_e (black bars) or τ_{loc} (gray bars), and (C) exchange contribution to nitrogen transverse relaxation at 61 MHz, $R_{ex} = R_2^{measured} - R_2^0$, calculated by fitting model-free equations to data at both fields simultaneously. Asterisks (*) indicate residues too severely exchange-broadened for measurement.

Structural studies show that little or no change in conformation occurs in the pseudo-EF hand (ψ-EF hand; residues 18−31) upon binding calcium. In contrast, the typical EF hand (residues 61−72) undergoes a dramatic Ca^{2+}-dependent change in the orientation of helix 3 to expose a hydrophobic patch of residues (*14*, *20*). Interestingly, helix 3 is the only helix with several residues having fast internal motion ($20 < \tau_e < 40$ ps for Q50, E51, and E62; $\tau_e = 800$ ps for T59; $\tau_e < 20$ ps for D54, V56, E58, and D61), and it has the lowest mean order parameter of the four helices (weighted mean $S^2 = 0.84$ versus 0.87, 0.86, and 0.87 for helices 1, 2, and 4, respectively). The lowest order parameters in helix 3 occur at its N- and C-termini (Q50, D61, and E62), and internal effective correlation times are detected mostly near the N-terminal end (Q50, E51, D54, and T59). Since helix 3 undergoes the largest dislocation upon addition of Ca^{2+}, perhaps this rapid motion facilitates the conversion from the apo conformation to the calcium-bound state. However, the absence of chemical exchange in helix 3 suggests that the motion in the C-terminal EF hand does not include the slower, large amplitude reorientation between the apo and calcium-loaded conformations.

As with their structures, the dynamics of the two EF hand Ca^{2+}-binding loops are quite different. In the ψ-EF hand (S18-E31), 3 out of the 13 measured order parameters are less than or equal to 0.8 (G22, D23, and K24), whereas 8 out of 11 measured order parameters (E62, D63, G64, D65, G66, E67, C68, and Q71) meet that criterion in the typical EF hand (D60−E72). In addition, rapid internal motion is detected ($\tau_e > 20$ ps) for only 6 of 14 residues (43%) in the pseudo-EF hand (R20, G22−H25, and K28), as compared

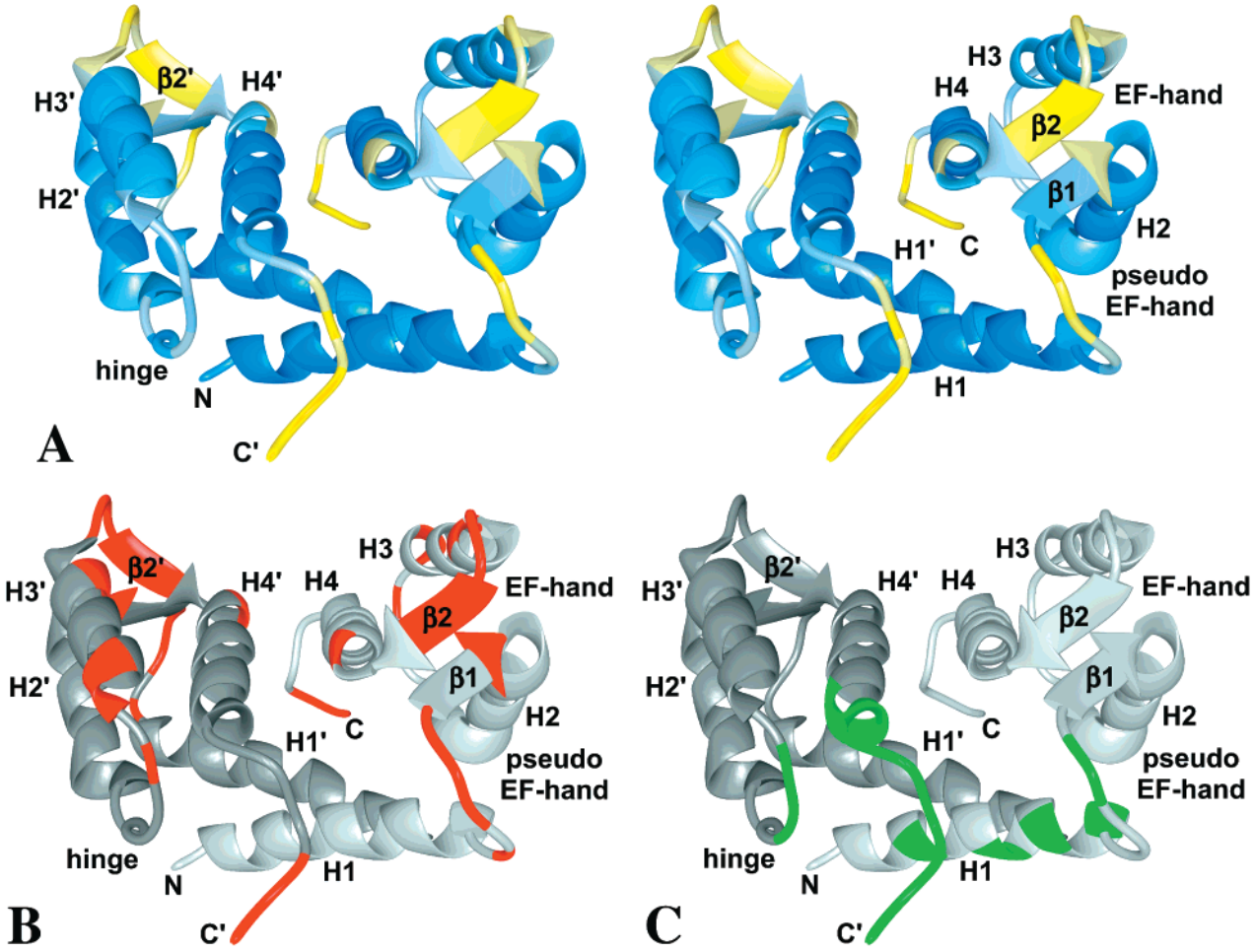

FIGURE 4: Model-free results for apo-S100B($\beta\beta$) mapped onto its three-dimensional structure. (A) Order parameters are shown in the stereo image on a gradient from blue (high S^2) to yellow (low S^2), (B) residues for which $\tau_e > 20$ ps are shown in red, and (C) residues for which $R_{ex} > 1$/s at 61 MHz nitrogen Larmor frequency are shown in green.

to 8 out of 12 residues (75%) in the calcium-binding domain of the typical EF hand (E62−C68, Q71; Figure 3, panel B, and Figure 4, panel B). While both EF hands have low order parameters in the center of the random coil portion of the EF hand (pseudo, G22, D23; typical, E62−D65), the β-strands show differences when the two Ca^{2+}-binding domains are compared. The three-residue β-strand in the lower-affinity ψ-EF hand (K26−K28) has higher order parameters (weighted mean 0.82) than the corresponding residues (E67−D69) of the typical EF hand (0.78), and the pattern of order parameters in strand 1 does not parallel that of strand 2. In the β-strand of the ψ-EF hand, a single low order parameter follows two higher values (strand 1, $S^2 =$ 0.85, 0.84, and 0.76, for K26, L27, and K28, respectively). In contrast, the corresponding segment of the typical EF hand has two lower order parameters followed by a single higher one (strand 2; $S^2 = 0.76$, 0.76, and 0.83 for E67, C68, and D69, respectively). This can be explained by the antiparallel alignment of the two strands in a small β-sheet, which brings together the pseudo- and typical EF hands. It is likely that the more mobile loop from the typical EF hand affects the motion of its own strand as well as the opposing strand in the sheet, as is also found for EF hands in the regulatory domain of cardiac troponin C (*47*). Although L27 and C68 share hydrogen bonds, significant motion is detected only at C68 ($S^2 = 0.76$, $\tau_s = 600$ ps), with little seen at L27 ($S^2 = 0.84$, $\tau_f < 20$ ps). The motion of the sheet may therefore be a twisting or rocking, centered roughly on the L27 amide H-N bond. Such motion would not be reflected in the L27 order parameter, but would be expected to affect the C68 value, whose amide-hydrogen bond vector is oriented about 20° differently than that of L27.

Loop 2, termed the hinge region and the C-terminal loop are the least conserved regions of the S100 protein family and directly interact with protein targets (*22*, *48*). The hinge is mostly a random-coil linker between the two calcium-binding motifs, and yet structure refinement through the use of dipolar couplings indicates that this linker is well-defined in the calcium-free state (*14*). We have confirmed this, showing that while order parameters in the hinge are lower on average than in adjacent helices, they are not uniformly so, and they are not as low as those observed in the calcium-binding loops, nor are local effective correlation times required to fit the data for the linker, except at K48 near helix 3, which displays such motions scattered throughout the helix. Although exchange is evident in this region at E46, I47, and K48, this does not necessarily imply motion in the loop. Rather, we propose that transient interactions with the C-terminal loop may be causing the observed chemical exchange because of the proximity and mobility of the C-terminus (Figure 4, panel C). As mentioned earlier, some weak NOEs have also been observed to support this.

Comparisons to Other EF Hand Proteins. Calbindin D_{9k} is the only other S100 protein that has had its backbone

dynamics analyzed using NMR relaxation data. Like S100B, it has an N-terminal pseudo-EF hand and a C-terminal typical EF hand, but it exists in solution as a monomer rather than a dimer as found for S100B. Also, calbindin does not undergo significant structural rearrangement on binding calcium (*49*, *50*), and its C-terminus is much shorter (by 11 residues) than that of S100B.

A comparison of order parameters between the calcium-binding regions of apo-S100B and apo-calbindin reveals some similarities, but in general, a more dramatic (10−15%) decrease in order is reported for calbindin in these loops. In calbindin, the minimum order parameter (S^2) in the typical EF hand is about 0.6, as compared to 0.73 for S100B. This result occurs despite the higher temperature used for the S100B study (37 °C, as compared to 27 °C for calbindin) and despite that we used a value for ^{15}N chemical shift anisotropy (−170 ppm), which would tend to give slightly lower order parameters than would the value (−160 ppm) used in the calbindin study (*25*). In contrast to S100B, the linker of calbindin is reported to be quite mobile, with order parameters as low as 0.5 for G42 and G43 (*25*). Interestingly, the linker in calbindin is shorter by three residues than in S100B, and for S100B there is a large rearrangement in the linker when Ca^{2+} and target proteins bind (*8*, *22*, *48*). For calbindin, the linker does become more ordered when Ca^{2+} binds. Finally, the ability of S100B to bind protein targets is critically dependent on the C-terminal loop (*51*, *52*). It is likely that much of the dynamic character of this loop is lost upon binding protein targets since exchange-broadening effects are eliminated in this region when a target peptide binds (*22*, *48*). In contrast, calbindin does not have this C-terminal extension, and it does not bind any known protein target. Therefore, despite the similar characteristics of the two EF hands in apo-S100B and apo-calbindin, the backbone dynamics of the two proteins are different, as are their functions, Ca^{2+}-buffering for calbindin vs. signaling for S100B.

Another protein containing the EF hand motif is skeletal troponin C (sTnc). sTnC has two domains, each with a pair of typical EF hands. The N-terminal regulatory domain (sNTnC) binds two calcium ions sequentially, with dissociation constants of 1.7 μM for site 2 (C-terminal) and 16 μM for site 1 (*53*). Upon binding calcium, sNTnC undergoes significant structural rearrangement, with the largest change of interhelical angle occurring between helices C and D (equivalent to 3 and 4 of S100B), about 60°, to form an "open" conformation. As for S100B, the open conformation of TnC is poised to bind its target (*54*). Although sTnC is not an S100 protein, its function as a signaling protein is similar to that of S100B, binding a target protein in a Ca^{2+}-dependent manner. The dynamics of S100B, likewise, parallel the dynamics of sNTnC more closely than those of calbindin (*55*). The highest order parameters of sNTnC are seen in all four EF hand helices with lower order parameters in the Ca^{2+}-binding loops. The short linker between the two EF hands displays moderately low order parameters at individual residues within the segment, but, as is the case for S100B, no overall decrease in order is present, arguing against extensive motion in this segment. Helix D of sNTnC serves much the same role in target-binding as helix 3 in S100B, reorienting to expose a hydrophobic patch upon binding calcium. However, helix D of sNTnC lacks the dynamical character of helix 3 of S100B.

CONCLUSIONS

S100B is a highly ordered protein with activated backbone dynamics in regions of the protein related to its function as a calcium-mediated signal transducer. Mobility in the calcium-free Ca^{2+}-binding loops is greater for the typical EF hand, which changes conformation on binding calcium in contrast to the "pseudo EF" or "S100" hand. This characteristic is similar to other EF hand proteins such as calbindin and TnC. Unlike calbindin, however, the hinge of S100B is actively involved in binding target proteins in the calcium-saturated state and was found to be relatively immobile in the calcium-free state. In this way, S100B is more like troponin C than calbindin. While small amounts of chemical exchange were observed in the hinge region, this exchange was attributed to the nearby motion of the extended and solvent-exposed C-terminus of S100B. Further studies to elucidate the dynamical contributions to the function of S100B should now focus on the calcium-saturated state, in the presence and absence of target.

ACKNOWLEDGMENT

The authors express their gratitude to Dr. A. G. Palmer of Columbia University for both software and invaluable advice. Molecular graphics images were produced using the MidasPlus package from the Computer Graphics Laboratory, University of California, San Francisco (supported by NIH P41 RR-01081).

SUPPORTING INFORMATION AVAILABLE

R_1, R_2, and NOE values, and their uncertainties, measured for apo-S100B($\beta\beta$) are available in two tables, S1 (14.1 T) and S2 (9.4 T). This material is available free of charge via the Internet at http://pubs.acs.org.

REFERENCES

1. Moore, B. (1965) *Biochem. Biophys. Res. Comm. 19*, 739−744.
2. Donato, R. (1991) *Cell Calcium 12*, 713−726.
3. Donato, R. (1999) *Biochim. Biophys. Acta. 1450*, 191−231.
4. Schäfer, B. W., and Heizmann, C. W. (1996) *Trends Biochem. Sci. 21*, 134−140.
5. Zimmer, D. B., Cornwall, E. H., Landar, A., and Song, W. (1995) *Brain Res. Bull. 37*, 417−429.
6. Weber, D. J., Rustandi, R. R., Carrier, F., and Zimmer, D. B. (2000) in *Calcium: The Molecular Basis of Calcium Action in Biology and Medicine* (Pochet, R., Donato, R., Haiech, J., Heizmann, C., and Gerke, V., Eds.) pp 521−539, Kluwer Academic Publishers, Dordrecht, The Netherlands.
7. Kligman, D., and Hilt, D. (1988) *Trends Biochem. Sci. 13*, 437−443.
8. Drohat, A. C., Baldisseri, D. M., Rustandi, R. R., and Weber, D. J. (1998) *Biochemistry 37*, 2729−2740.
9. Smith, S. P., and Shaw, G. S. (1998) *Structure 6*, 211−222.
10. Matsumura, H., Shiba, T., Inoue, T., Harada, S., Kai, Y. (1998) *Structure 6*, 233−241.
11. Kretsinger, R. H. (1980) *CRC Crit. Rev. Biochem. 8*, 119−174.
12. Strynadka, N. C. J., and James, M. N. G. (1989) *Annu. Rev. Biochem. 58*, 951−998.
13. Baudier, J., Glasser, N., and Gerard, D. (1986) *J. Biol. Chem. 261*, 8192−8203.

14. Drohat, A. C., Tjandra, N., Baldisseri, D. M., and Weber, D. J. (1999) *Protein Sci. 8*, 800−809.
15. Maler, L., Potts, B. C. M., and Chazin, W. J. (1999) *J. Biomol. NMR 13*, 233−247.
16. Rety, S., J., S., Renouard, M., Osterloh, D., Gerke, V., Tabaries, S., Russo-Marie, F., and Lewit-Bentley, A. (1999) *Nat. Struct. Biol. 6*, 89−95.
17. Drohat, A. C., Nenortas, E., Beckett, D., and Weber, D. J. (1997) *Prot. Sci. 6*, 1577−1582.
18. Groves, P., Finn, B. E., Kuznicki, J., and Forsen, S. (1998) *FEBS Lett. 421*, 175−179.
19. Smith, S. P., and Shaw, G. S. (1998) *Biochem. Cell Biol. 76*, 324−333.
20. Drohat, A. C., Rustandi, R. R., and Baldisseri, D. M. (1997) *Biochemistry 37*, 2729−2740.
21. Rustandi, R. R., Drohat, A. D., Baldisseri, D. M., Wilder, P. T., and Weber, D. J. (1998) *Biochemistry 37*, 1951−1960.
22. Rustandi, R. R., Baldisseri, D. M., and Weber, D. J. (2000) *Nat. Struct. Biol. 7*, 570−574.
23. Wilder, P. T., Rustandi, R. R., Drohat, A. C., and Weber, D. J. (1998) *Protein Sci. 7*, 794−798.
24. Kordell, J., Skelton, N. J., Akke, M., Palmer, A. P., III, and Chazin, W. J. (1992) *Biochemistry 31*, 4856−4866.
25. Akke, M., Skelton, N. J., Kordel, J., Palmer, A. G. I., and Chazin, W. J. (1993) *Biochemistry 32*, 9832−9844.
26. Inman, K., Baldisseri, D. M., and Weber, D. J. (1998) *FASEB J. 12*, 732.
27. Farrow, N. A., Ranjith, M., Singer, A. U., Pascal, S. M., Kay, C. M., Gish, G., Shoelson, S. E., Pawson, T., Forman-Kay, J. D., and Kay, L. E. (1994) *Biochemistry 33*, 5984−6003.
28. Delaglio, F., Grzesiek, S., Vuister, G. W., Zhu, G., Pfeifer, J., and Bax, A. (1995) *J. Biomol. NMR 6*, 277−293.
29. Mosteller, F., and Tukey, J. W. (1977) *Data Analysis and Regression: A Second Course in Statistics*, Addison-Wesley, Reading, MA.
30. Press, W. H., Teukolsky, S. A., Vetterling, W. T., and Flannery, B. P. (1992) *Numerical Recipes in Fortran 77: The Art of Scientific Computing*, Vol. 1, 2nd ed., Cambridge University Press, New York.
31. Kay, L. E., Torchia, D. A., and Bax, A. (1989) *Biochemistry 28*, 8972−8979.
32. Brüschweiler, R., Liao, X., and Wright, P. E. (1995) *Science 268*, 886−889.
33. Tjandra, N., Wingfield, P., Stahl, S., and Bax, A. (1996) *J. Biomol. NMR 8*, 273−284.
34. Lee, L. K., Rance, M., Chazin, W. J., and Palmer, A. G. (1997) *J. Biomol. NMR 9*.
35. Lipari, G., and Szabo, A. (1982) *J. Am. Chem. Soc. 104*, 4546−4559.
36. Lipari, G., and Szabo, A. (1982) *J. Am. Chem. Soc. 104*, 4559−4570.
37. Clore, G. M., Szabo, A., Bax, A., Kay, L. E., Driscoll, P. C., and Gronenborn, A. M. (1990) *J. Am. Chem. Soc. 112*, 4989−4991.
38. Barbato, G., Ikura, M., Kay, L. E., Pastor, R. W., and Bax, A. (1992) *Biochemistry 31*, 5269−5278.
39. Abragam, A. (1961) *The Principles of Nuclear Magnetism*, 1st ed., corrected 1970 ed., Oxford University Press, London, U.K.
40. Lee, A. L., and Wand, A. J. (1999) *J. Biomol. NMR 13*, 101−112.
41. Mandel, A. M., Akke, M., and Palmer, A. G. (1995) *J. Mol. Biol. 246*, 144−163.
42. Palmer, A. G., Rance, M., and Wright, P. E. (1991) *J. Am. Chem. Soc. 113*, 4371−4381.
43. de Alba, E., Baber, J. L., and Tjandra, N. (1999) *J. Am. Chem. Soc. 121*, 4282−4283.
44. van Holde, K. E. (1985) *Physical Biochemistry*, 2nd ed., Prentice-Hall, Inc., Englewood Cliffs, N. J.
45. Brüschweiler, R., and Wright, P. E. (1994) *J. Am. Chem. Soc. 116*, 8426−8427.
46. Andrec, M., Inman, K. G., Weber, D. J., Levy, R. M., and Montelione, G. T. (2000) *J. Magn. Res. 146*, 66−80.
47. Spyracopoulos, L., Gagne, S. M., Li, M. X., and Sykes, B. D. (1998) *Biochemistry 37*, 18032−18044.
48. Rustandi, R. R., Baldisseri, D. M., Drohat, A. C., and Weber, D. J. (1999) *Protein Sci. 8*, 1743−1751.
49. Skelton, N. J., Kördel, J., Forsen, S., and Chazin, W. J. (1990) *J. Mol. Biol. 213*, 593−598.
50. Skelton, N. J., Kördel, J., and Chazin, W. J. (1995) *J. Mol. Biol. 249*, 441−462.
51. Garbuglia, M., Verzini, M., Rustandi, R. R., Osterloh, D., Weber, D. J., Gerke, V., and Donato, R. (1999) *Biochem. Biophys. Res. Commun. 254*, 36−41.
52. Landar, A., Rustandi, R. R., Weber, D. J., and Zimmer, D. B. (1998) *Biochemistry 37*, 17429−17438.
53. Li, M. X., Gagné, S. M., Tsuda, S., Kay, C. M., Smillie, L. B., and Sykes, B. D. (1995) *Biochemistry 34*, 8330−8340.
54. Gagné, S. M., Tsuda, S., Li, M. X., Smillie, L. B., and Sykes, B. D. (1995) *Nat. Struct. Biol. 2*, 784−789.
55. Gagné, S. M., Tsuda, S., Spyracopoulos, L., Kay, L. E., and Sykes, B. D. (1998) *J. Mol. Biol. 278*, 667−686.

BI0027478